High Temperature Stability of Onion-Like Carbon vs Highly Oriented Pyrolytic Graphite

Alessandro Latini[1], Massimo Tomellini[2], Laura Lazzarini[3], Giovanni Bertoni[3], Delia Gazzoli[1], Luigi Bossa[1], Daniele Gozzi[1]*

1 Dipartimento di Chimica, Università di Roma La Sapienza, Roma, Italy, 2 Dipartimento di Scienze e Tecnologie Chimiche, Università di Roma Tor Vergata, Roma, Italy, 3 IMEM – CNR, Parma, Italy

Abstract

The thermodynamic stability of onion-like carbon (OLC) nanostructures with respect to highly oriented pyrolytic graphite (HOPG) was determined in the interval 765–1030 K by the electromotive force (emf) measurements of solid electrolyte galvanic cell: (Low) $Pt|Cr_3C_2,CrF_2,OLC|CaF_2 s.c.|Cr_3C_2,CrF_2,HOPG|Pt$ (High). The free energy change of transformation HOPG = OLC was found positive below 920.6 K crossing the zero value at this temperature. Its trend with temperature was well described by a 3rd degree polynomial. The unexpected too high values of $\left(\frac{\partial \Delta_r H_T}{\partial T}\right)_P = \Delta c_P(T)$ jointly to the HR-TEM, STEM and EELS evidences that showed OLC completely embedded in rigid cages made of a Cr_3C_2/CrF_2 matrix, suggested that carbon in the electrodes experienced different internal pressures. This was confirmed by the evaluation under constant volume of $\frac{dP}{dT}$ by the $\frac{\alpha}{\kappa}$ ratio for OLC (0.5 MPa K^{-1}) and HOPG (8 Pa K^{-1}) where α and κ are the isobaric thermal expansion and isothermal compressibility coefficients, respectively. The temperature dependency of the pressure was derived and utilized to calculate the enthalpy and entropy changes as function of temperature and pressure. The highest value of the internal pressure experienced by OLC was calculated to be about 7 GPa at the highest temperature. At 920.6 K, $\Delta_r H$ and $\Delta_r S$ values are 95.8 kJ mol^{-1} and 104.1 JK^{-1} mol^{-1}, respectively. The surface contributions to the energetic of the system were evaluated and they were found negligible compared with the bulk terms. As a consequence of the high internal pressure, the values of the enthalpy and entropy changes were mainly attributed to the formation of carbon defects in OLC considered as multishell fullerenes. The change of the carbon defect fraction is reported as a function of temperature.

Introduction

The modifications of the internal arrangements and related energies of single wall carbon nanotubes (SWCNTs) in bundles were studied [1] by our group in the particular situation where their dilatation due to the high temperatures was hindered being the bundles embedded in a matrix much less dilatable. This generates high internal pressures, which are a direct consequence of the increase of the internal energy of the system producing changes in the SWCNT configuration inside the bundle and deformation of SWCNTs too.

The knowledge of the thermodynamic stability of nanostructures is a fundamental aspect to design new nanostructured materials as well as to forecast their behaviour. Most of the information on this subject comes from computational studies [2][3][4][5][6] and to a lesser extent by experimental works [7][8][9]. To the best of author knowledge and with the exception of reference [10][11][12] there are no articles dealing with

thermodynamic measurements at high temperature on carbon nanostructures.

On the other hand, the 3D carbon phase diagram, where the third axis is the particle size, is still under consideration. The contribution of the surface energy to the bulk Gibbs free energy per atom of a cluster of n atoms in a given phase is strongly affected by the number of atoms itself. In general, a review of the literature regarding the structure of carbon nanoparticles [13] highlights that at sizes below 1.8 nm, other carbon forms are abundant, such as fullerenes and onion-like carbon (OLC). Therefore, Kuznetsov et al. [14] suggested to assign a corresponding region of the phase diagram to closed-shell sp^2-bonded nanocarbons. In their phase diagram the regions of stability are specifically indicated for fullerenes and OLC for $n = 10$ to 10^2 atoms. The complete and thorough vision of the phase diagrams of these nanostructures in comparison with the phase diagram of the corresponding bulk materials has not been realized yet. There is still a great deal of work to be done in the construction of a

complete *P–T–n* phase diagram of carbon. It is likely however that knowledge gained from theoretical and computational studies [15] of nanocarbon stability plays an important role in the conception of such a diagram, with thermodynamic treatments of phase equilibrium showing the right way for pursuing the final goal.

Onion-like carbon are another class of carbon nanostructures, which are not exhaustively investigated yet though some published results envisage interesting applications such as an easy route to produce diamond nanoparticles [7][8][16] as well as to use them as reaction cells on the nanoscale [9].

The scope of this work is to study, in conditions of reversibility, the thermodynamics of the high temperature transformation under volume constraint from highly oriented pyrolytic graphite (HOPG) to OLC.

Experimental

Since the experimental set-up was published elsewhere [10][11][12] and there is the will of the authors to give in this paper more room to the chemical thermodynamics of our experiment and discussion of the results, we decided to describe more in details the wide experimental part in the Supporting Information S1. A list of all the aspects that took part to the whole experimentation of this work, which are reported in the Supporting Information S1, follows:

1. Starting materials for the electrode preparation
   1.1. HOPG, OLC, Cr_3C_2, CrF_2
   1.2. Characterization
      1.2.1. Thermogravimetry (TG) and Differential Thermal Analysis (DTA)
      1.2.2. x-ray diffraction (XRD)
      1.2.3. microRaman (mR)
      1.2.4. High Resolution Transmission Electron Spectroscopy (HR-TEM)
      1.2.5. Electron Energy Loss Spectroscopy (EELS)
      1.2.6. X-ray Photoelectron Spectroscopy (XPS)
   1.3. Preparation of electrodes and cell assembly
      1.3.1. Electrodes
      1.3.2. Cell assembly
   1.4. Experimental apparatus for the *emf* measurements
   1.5. Procedure adopted for the *emf* measurements and their data acquisition
   1.6. Analysis of electrodes before and after experiment
      1.6.1. X-ray diffraction (XRD)
      1.6.2. microRaman spectroscopy (mR)
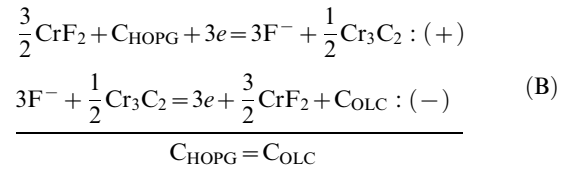   1.6.3. EELS

Results and Discussion

In order to satisfy the requirement of reversibility, the experimental technique utilized is the electromotive force (*emf*) measurement as function of temperature of galvanic cells, with CaF_2 single crystal as solid electrolyte. Since long time this technique was utilized in our laboratory and it is well known that the method is one of the best way to achieve reliable thermodynamic data.

The galvanic cell:

(Low) $Pt | Cr_3C_2, CrF_2, OLC | CaF_2 \, s.c. | Cr_3C_2, CrF_2, HOPG | Pt$ (High) (A)

was assembled to perform the *emf* vs *T* measurement. Cell A is a fluorine concentration cell being the solid electrolyte an ionic conductor by F⁻ Frenkel type defects. The positive electrode is the electrode where the chemical potential of $F_2(g)$ is higher and the

chemical potential of carbon is lower. This implies that $\Delta\mu_C = -\frac{3}{2}\Delta\mu_{F_2}$. The cell reaction can be written as:

$$\frac{3}{2}CrF_2 + C_{HOPG} + 3e = 3F^- + \frac{1}{2}Cr_3C_2 : (+)$$

$$\frac{3F^- + \frac{1}{2}Cr_3C_2 = 3e + \frac{3}{2}CrF_2 + C_{OLC} : (-)}{C_{HOPG} = C_{OLC}} \quad \text{(B)}$$

The main advantage of this kind of cells is that no supplementary thermodynamic data are necessary to derive the thermodynamics of the cell reaction. Only the *emf* vs *T* experimental data are necessary to obtain the reaction Gibbs free energy change, $\Delta_r G$. The reaction changes of enthalpy, $\Delta_r H$, and entropy, $\Delta_r S$, can be also obtained as shown in the followings.

The adopted experimental procedure requires accumulating many isothermal and stationary values of *emf* through several stair shaped thermal cycles each one composed of tens of isotherms. Figure 1 shows the typical behaviour, almost equal for each one, of five tested cells. The first thermal cycles are characterized by hysteresis that tends to disappear. The presence of a vanishing hysteresis in the *emf* trend demonstrates that the whole system of the carbon shells in the OLC and OLC themselves change to reach new stable configurations that convert reciprocally and reversibly as function of temperature. These findings are qualitatively and quantitatively similar to the behaviour we found in the bundles of SWCNTs [1]. The main difference with the present experiment is the final shape of the *emf* vs *T* curve that is characterized here by an exponential growth-like behaviour.

The trend of the Gibbs free energy change is given by:

$$\Delta_r G_T = -3\mathcal{F}E(T) \quad (1)$$

being 3 the number of moles of electrons exchanged in reaction B and $\mathcal{F}$ the Faraday constant. The curve $E(T)$ is well fit by the 3rd degree polynomial:

$$E(T) = a + bT + cT^2 + dT^3 \quad (2)$$

.The coefficients and related errors of fit of *emf* vs *T* are given in Table 1. The representation of eq 1 is given in Fig. 2 where at 920.6 K the equality of the chemical potential of carbon $\mu_C(HOPG) = \mu_C(OLC)$ is satisfied.

If each point of the curve of Fig. 2 were a point taken at constant temperature and pressure, the enthalpy change of the transformation, $\Delta_r H_T$, would be given by:

$$\Delta_r H_T = -3\mathcal{F}\left[E(T) - T\left(\frac{\partial E}{\partial T}\right)_P\right] \quad (3)$$

The temperature dependency of eq 3 should be written as given in any chemical thermodynamics textbook by equation:

$$\left(\frac{\partial \Delta_r H_T}{\partial T}\right)_P = 3\mathcal{F}T\left(\frac{\partial^2 E}{\partial T^2}\right)_P = \Delta c_P(T) \quad (4)$$

being $\Delta c_P(T) = c_P(OLC) - c_P(HOPG)$ and c_P the molar heat capacity at constant pressure. In the case of reaction B and at the experimental temperatures, it is expected that $\Delta c_P(T)$ should be
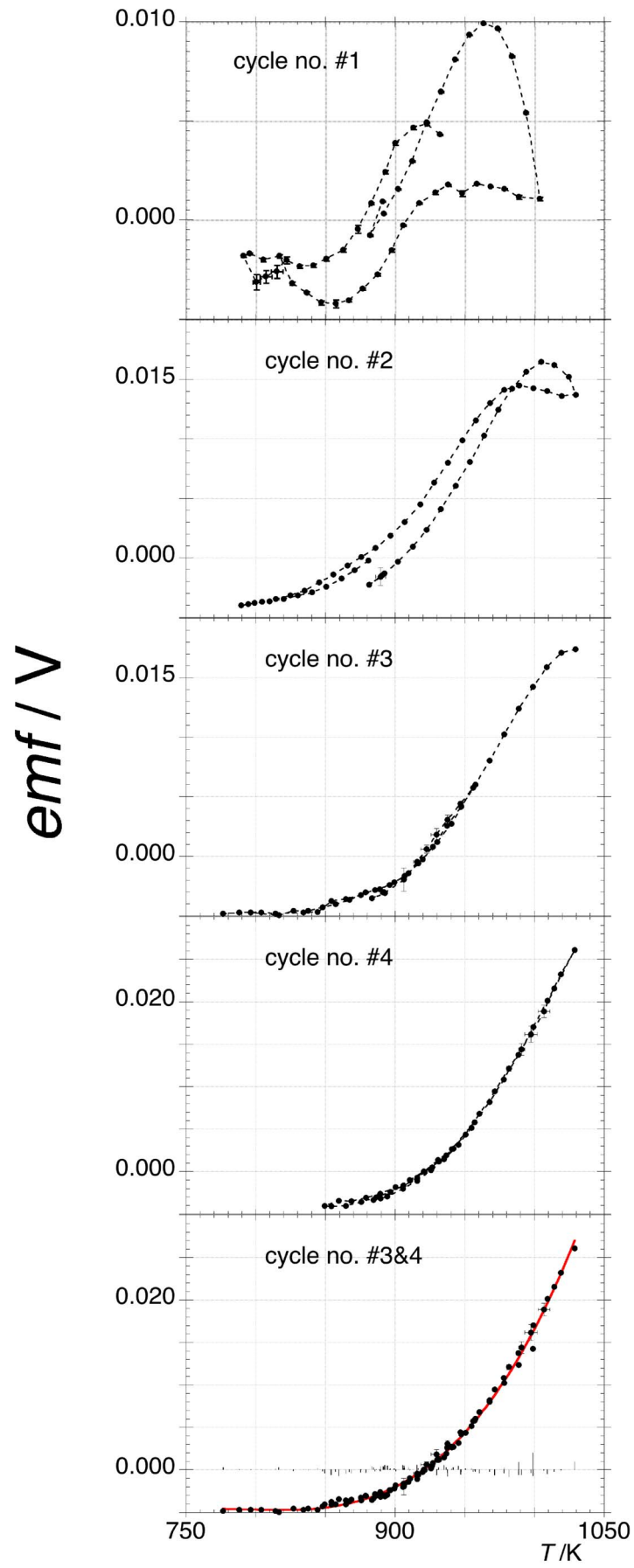
Figure 1. The electromotive force (*emf*) vs temperature of galvanic cell A. The progressive disappearing hysteresis is shown from 1st to 3rd thermal cycle (see §1.4 of the Supporting Information S1). The bottom plot combines the 3rd and 4th cycles where the red curve is the best fitting curve given by a 3rd degree polynomial (see Table 1). The residuals of fit are also reported. Most of the error bars are within the size of the experimental points.

quite low. Equation 4 implies the same value of pressure at each temperature for both the electrodes, i.e., $\left(\frac{\partial \Delta_r H_T}{\partial T}\right)_P = \frac{d\Delta_r H_T}{dT}$. The 1st partial derivative against T of eq 3, i.e. eq 4, shows too high $\Delta c_V(T)$ values which are unexpected for the process under study. For this reason, the assumption of constant pressure is not more valid. Therefore, the total derivative of $E(T)$, i.e.,

$$\frac{dE}{dT} = \left(\frac{\partial E}{\partial T}\right)_P + \left(\frac{\partial E}{\partial P}\right)_T \frac{dP}{dT} \qquad (5)$$

should be considered where,

$$\left(\frac{\partial E}{\partial P}\right)_T = -\frac{1}{3\mathcal{F}}\left(\frac{\partial \Delta_r G_T}{\partial P}\right)_T = -\frac{1}{3\mathcal{F}}\Delta V \qquad (6)$$

being $\Delta V = V(\text{OLC}) - V(\text{HOPG})$ and V is the molar volume. By substituting eq 6 in eq 5 and combining with eq 3, the P, T dependency of $\Delta_r H_T = -3\mathcal{F}\left\{E(T,P) - T\left[\frac{dE}{dT} + \frac{\Delta V}{3\mathcal{F}}\frac{dP}{dT}\right]\right\}$ is found:
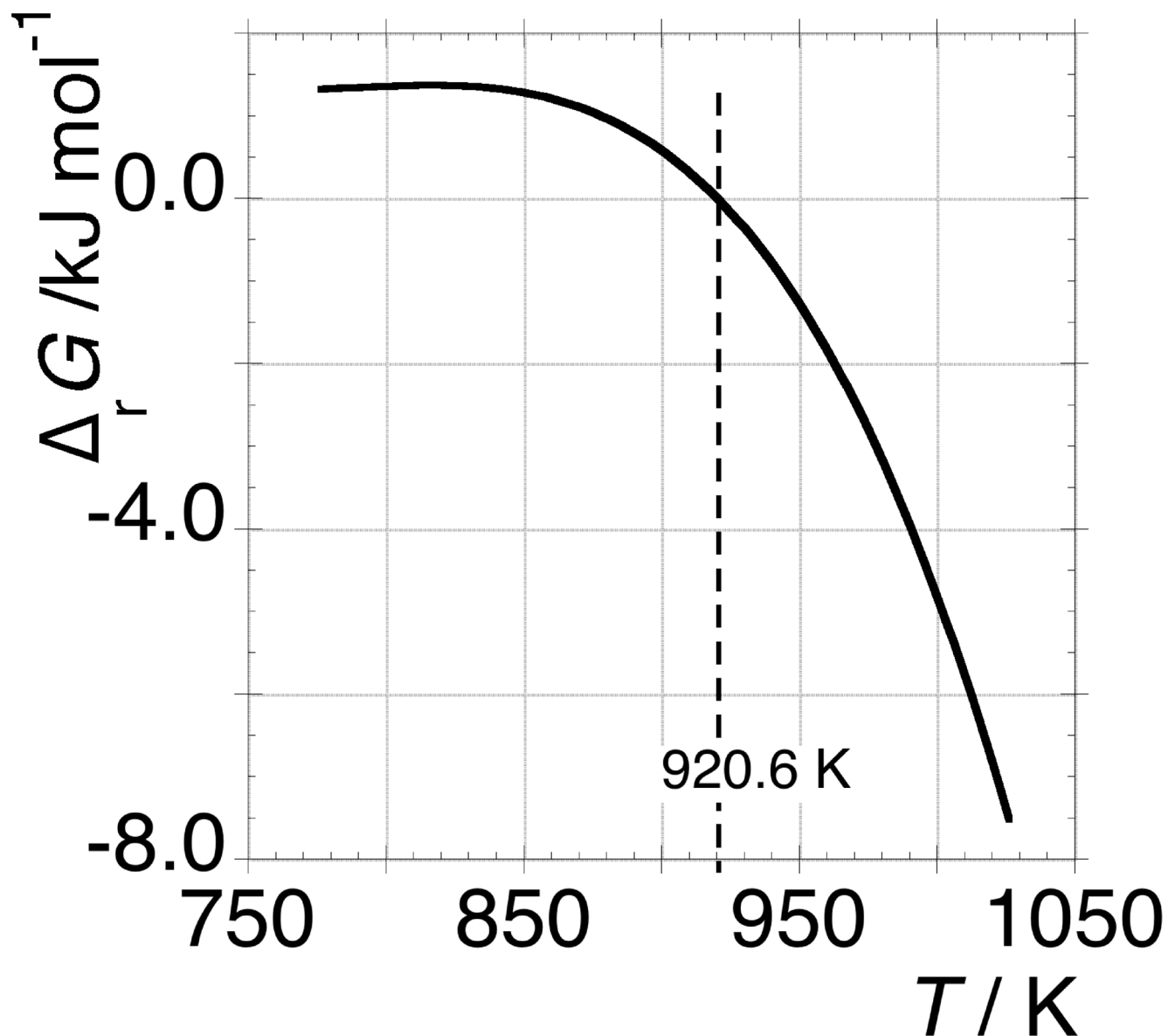

Figure 2. Gibbs free energy change for $C_{HOPG} = C_{OLC}$ transformation calculated according to eq 1. At 920.6 K, the curve crosses zero.

Table 1. Coefficients and related errors of *emf* vs *T* polynomial fit: $E(T) = a + bT + cT^2 + dT^3$.

	a/V	b/VK^{-1}	c/VK^{-2}	d/VK^{-3}
coefficient	-1.207	0.0045698	-5.7832×10^{-6}	2.437×10^{-9}
error	0.12433	0.0004144	4.5905×10^{-7}	1.691×10^{-10}

$R = 0.99836$; $\chi^2 = 1.5935 \times 10^{-5}$.
doi:10.1371/journal.pone.0105788.t001

$$\Delta_r H_T = -3\mathcal{F} \left\{ E(T,P) - T \left[\frac{dE}{dT} + \frac{\Delta V}{3\mathcal{F}} \frac{dP}{dT} \right] \right\} \quad (7)$$

Accordingly, eq 7 differs from eq 3 for the extra term $\left(T \frac{\Delta V}{3\mathcal{F}} \frac{dP}{dT} \right)$, which entails $\frac{dE}{dT} \neq \left(\frac{\partial E}{\partial T} \right)_P$.

The 1st derivative of eq 7 with respect to T is:

$$\frac{d\Delta_r H}{dT} = 3\mathcal{F} T \frac{d^2 E}{dT^2} + T \frac{d\Delta V}{dT} \frac{dP}{dT} + \Delta V \frac{dP}{dT} + T \Delta V \frac{d^2 P}{dT^2} . \quad (8)$$

From the total differential of $\Delta V(T,P)$, the relationship below follows:

$$\frac{d\Delta V}{dT} = \left(\frac{\partial \Delta V}{\partial T} \right)_P + \left(\frac{\partial \Delta V}{\partial P} \right)_T \frac{dP}{dT} = \Delta(\alpha V) - \frac{dP}{dT} \Delta(\kappa V) \quad (9)$$

where α and κ are, respectively, the isobaric volume expansion coefficient and isothermal compressibility. By making use of eq 9, eq 8 can be conveniently modified in the form:

$$\frac{d\Delta_r H}{dT} = 3\mathcal{F} T \frac{d^2 E}{dT^2} \left\{ T \frac{dP}{dT} \left[\Delta(\alpha V) - \frac{dP}{dT} \Delta(\kappa V) \right] \right\} + \Delta V \frac{dP}{dT} + T \Delta V \frac{d^2 P}{dT^2} \quad (10)$$

Equation 10 should be compared with well-known equation [17]:

$$\frac{d\Delta_r H}{dT} = \Delta c_P(T) + [\Delta V - T \Delta(\alpha V)] \frac{dP}{dT} \quad (11)$$

which states that if some phase transition occurs, the equilibrium pressure does not remain constant as the temperature is varied. Since we can write that $\Delta c_P(T) = \Delta c_V(T) + T \Delta \left(\frac{\alpha^2 V}{\kappa} \right)$, by equating eq 10 and eq 11, the following 2nd order differential equation for P is found:

$$\Delta V \frac{d^2 P}{dT^2} - \Delta(\kappa V) \left(\frac{dP}{dT} \right)^2 + 2\Delta(\alpha V) \frac{dP}{dT} + 3\mathcal{F} \frac{d^2 E}{dT^2} - \frac{\Delta c_V}{T} - \Delta \left(\frac{\alpha^2 V}{\kappa} \right) = 0 \quad (12)$$

To simplify eq 12, we can reasonably neglect $\frac{d^2 P}{dT^2}$ and assume $\Delta c_V \cong 0$ being both OLC and HOPG graphitic materials at the same quite high temperature where c_V is for both ones close to $\frac{3}{2} R$. Therefore, eq 12 becomes a quadratic equation in the 1st derivative with respect to T of the pressure:

$$\left(\frac{dP}{dT} \right)^2 - 2 \frac{\Delta(\alpha V)}{\Delta(\kappa V)} \frac{dP}{dT} - \frac{1}{\Delta(\kappa V)} \left[3\mathcal{F} \frac{d^2 E}{dT^2} - \Delta \left(\frac{\alpha^2 V}{\kappa} \right) \right] \cong 0 \quad (13)$$

The solution of eq 13 has been obtained by using the experimental data, $\frac{d^2 E}{dT^2}$, and the knowledge of the T and P functions of the physical data of HOPG and OLC. The T functions are reported in Table 2 and their related coefficients given in Table 3. Unfortunately, α and κ data of OLC are unavailable and we utilized, as first approximation, the data of fullerene C_{60} [18]. Due to lack of data on the temperature dependency of the OLC molar volume, an estimation can be done starting from the definition of the isobaric expansion coefficient $\alpha(T) = \frac{1}{V} \left(\frac{\partial V}{\partial T} \right)_P$ and its T dependency reported in Table 2 together the coefficients for C_{60} given in Table 3. Therefore, equation below has been considered:

$$V(T) = V(T_0) \exp \left[\int_{T_0}^{T} (d_0 + d_1 T) dT \right]$$
$$= V(T_0) \exp \left\{ \Delta T \left[d_0 + \frac{d_1}{2} (T + T_0) \right] \right\} \cong V(T_0) \quad (14)$$

where $\left(T^2 - T_0^2 \right) = \Delta T (T + T_0)$ holds. The final approximated value is justified by the amount in braces, which is $\cong 3 \times 10^{-2}$ being $\Delta T = (T - T_0) \leq 700 K$. The values of d_0 and d_1 are reported in Table 3. The $V(T_0)$ value was taken equal to 7.31×10^{-6} m^3 mol^{-1} at $T_0 = 298$ K which is the V^0 value of OLC [19]) (see Table 3). Due to the lack of data on the pressure dependence of α, κ and V^0 for OLC, all these parameters were considered constant with pressure for the carbon species present in both electrodes. This choice was mandatory to ensure a balanced behaviour to both OLC and HOPG. Figure 3 shows the trend of $\frac{d\Delta_r H_T}{dT}$ vs T in the left axis calculated according to eq 11 after solving eq 13 to find $\frac{dP}{dT}$, being the latter quantity plotted on the right axis. It should be noticed that the shape of the curve $\frac{dP}{dT}$ might be affected by the approximation $\frac{d^2 P}{dT^2} \cong 0$ introduced in equation 12.
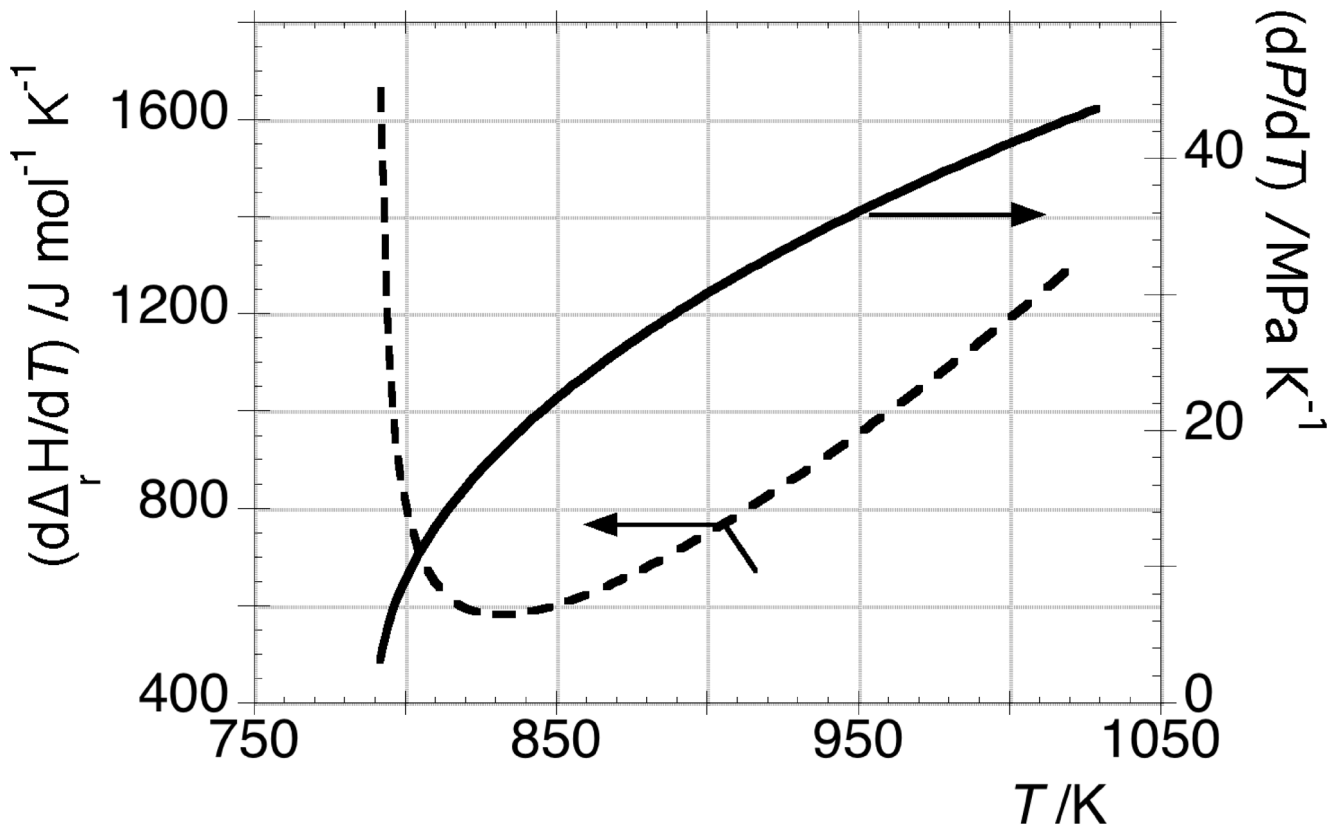
Figure 3. Representation of $\frac{dP}{dT}$ vs T obtained by solving eq 13 (right axis) and trend of $\Delta_r H(P,T)$ calculated by eq 11 (left axis).
doi:10.1371/journal.pone.0105788.g003

From the total differential of $\Delta_r H(T,P)$ the quantity

$$\left(\frac{\partial \Delta_r H}{\partial P}\right)_T = \frac{\dfrac{d\Delta_r H}{dT} - \left(\dfrac{\partial \Delta_r H}{\partial T}\right)_P}{\dfrac{dP}{dT}}$$ can be obtained and plotted

against T in Fig. 4 (right axis) together $\left(\dfrac{\partial \Delta_r H_T}{\partial T}\right)_P$ (left axis).
Equation 4 was used for this calculation.

The entropy change of transformation B as function of temperature and pressure, was calculated as:

$$\Delta_r S(T,P) = [\Delta_r H(T,P) - \Delta_r G(T,P)]/T \qquad (15)$$

.This equation can be calculated through eq 7, after solving the quadratic eq 13, by using the experimental data of $\Delta_r G$ reported

on Fig. 2. These thermodynamic functions are shown in Fig. 5. At 920.6 K, $\Delta_r H$ and $\Delta_r S$ values are 95.8 kJ mol^{-1} and 104.1 JK^{-1} mol^{-1}, respectively.

Why does the pressure change with temperature in our experiment? The experiment is carried out under high vacuum and the static pressure on the cell is maintained constant at about 0.1 bar as described in the experimental section (see § 1.3 of the Supporting Information S1). Thus, the present experimental conditions cannot justify the presence of the $\dfrac{dP}{dT}$ quantity. The explanation for $\dfrac{dP}{dT} >> 0$ should be searched in the growth of the pressure inside the cell, which is caused by a process occurring under volume constraint. The positive sign of *emf* indicates that $\mu(\text{OLC}) > \mu(\text{HOPG})$ where μ is the chemical potential of carbon. By itself this does not justify the increase of P with T but the trend of *emf* with T suggests it. Furthermore, there are experimental

Table 2. Temperature functions of the molar volume, V^0, isobaric volume expansion coefficient, α, and isothermal compressibility, κ, used for computing eq 13.

	$V^0(T)$[a]	$\alpha(T)$[b]	$\kappa(T)$[b]
HOPG[25]	$a_1 + a_2 T + a_3 T^2$	$\dfrac{a_2 + 2a_3 T}{a_1 + a_2 T + a_3 T^2}$	$\left(b_1 + b_2 T + b_3 T^2\right)^{-1}$
OLC	V^0	$d_0 + d_1 T$	$c_0 + c_1 T$

[a]Fullerene C$_{60}$ data were assumed for OLC from reference [18] (see also text) with the exception of $\dfrac{dP}{dT}$, which is known [19].
[b]Linear equations for OLC (C$_{60}$) were taken up from the plots in reference [18].
doi:10.1371/journal.pone.0105788.t002

Table 3. Values of the coefficients of Table 2.

Coefficient [a]	Value	Ref.
$a_1/\text{m}^3\text{mol}^{-1}$	5.30×10^{-6}	[25]
$a_2/\text{m}^3\text{ mol}^{-1}\text{K}^{-1}$	2.14×10^{-10}	[25]
$a_3/\text{m}^3\text{ mol}^{-1}\text{K}^{-2}$	1.95×10^{-14}	[25]
b_1/Pa	3.63×10^{10}	[25]
$b_2/\text{Pa K}^{-1}$	-1.32×10^{7}	[25]
$b_3/\text{Pa K}^{-2}$	9.45×10^{3}	[25]
c_0/Pa^{-1}	8.37×10^{-11}	[18]
$c_1/\text{Pa}^{-1}\text{K}^{-1}$	7.66×10^{-15}	[18]
d_0/K^{-1}	4.30×10^{-5}	[18]
d_1/K^{-2}	4.27×10^{-9}	[18]
$V^0/\text{m}^3\text{mol}^{-1}$	7.31×10^{-6}	[19]

[a]The original values of coefficients α_i are given in nm^3. They were multiplied by 10^{-27} N_A being N_A the Avogadro number.
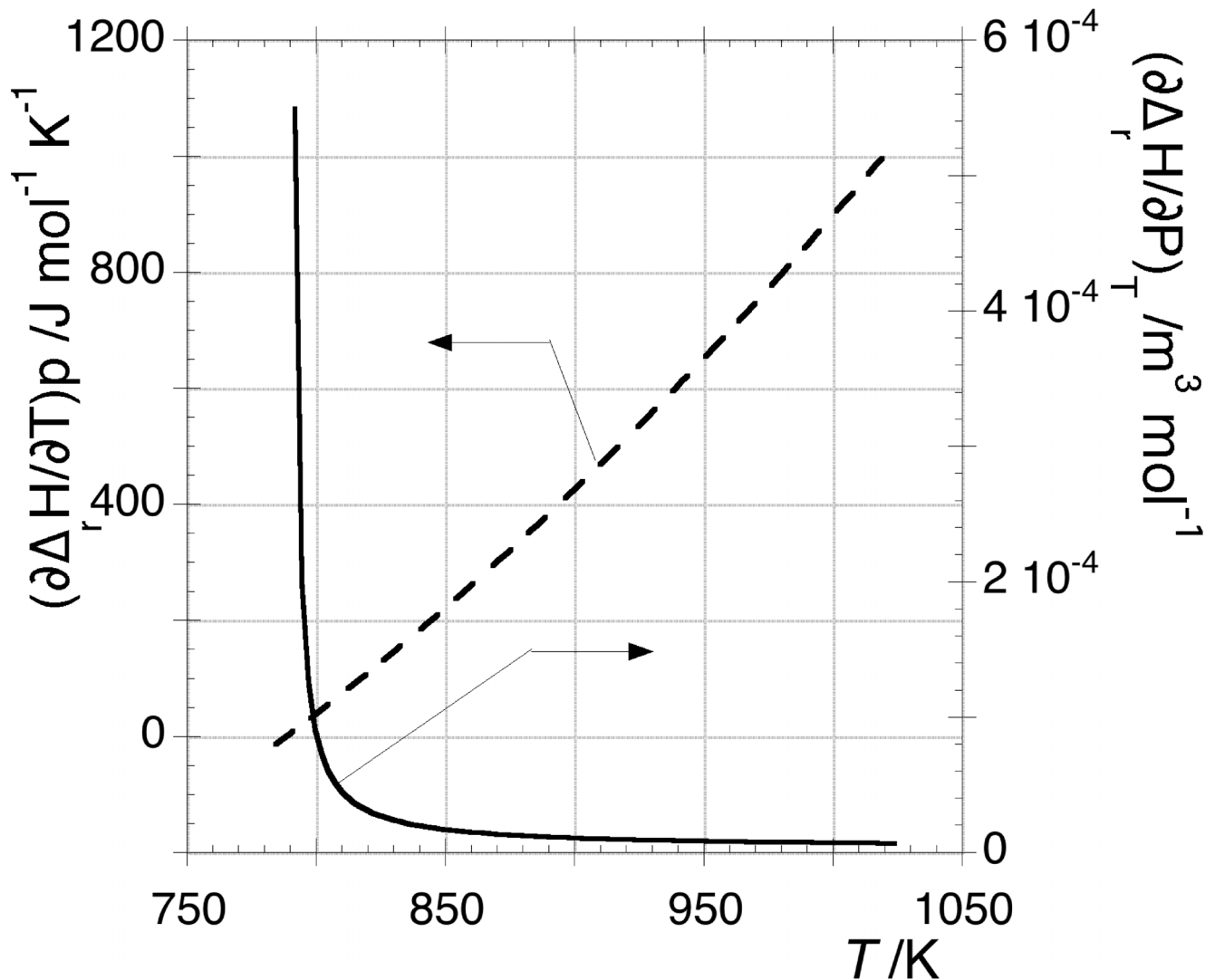
doi:10.1371/journal.pone.0105788.t003

Figure 4. Partial derivatives of $\Delta_r H(P,T)$. The quantity in the left axis was calculated according to eq 4. The quantity in the right axis was calculated by the total differential of $\Delta_r H(P,T)$ through $\frac{dP}{dT}$ vs T function, obtained by solving eq 13.

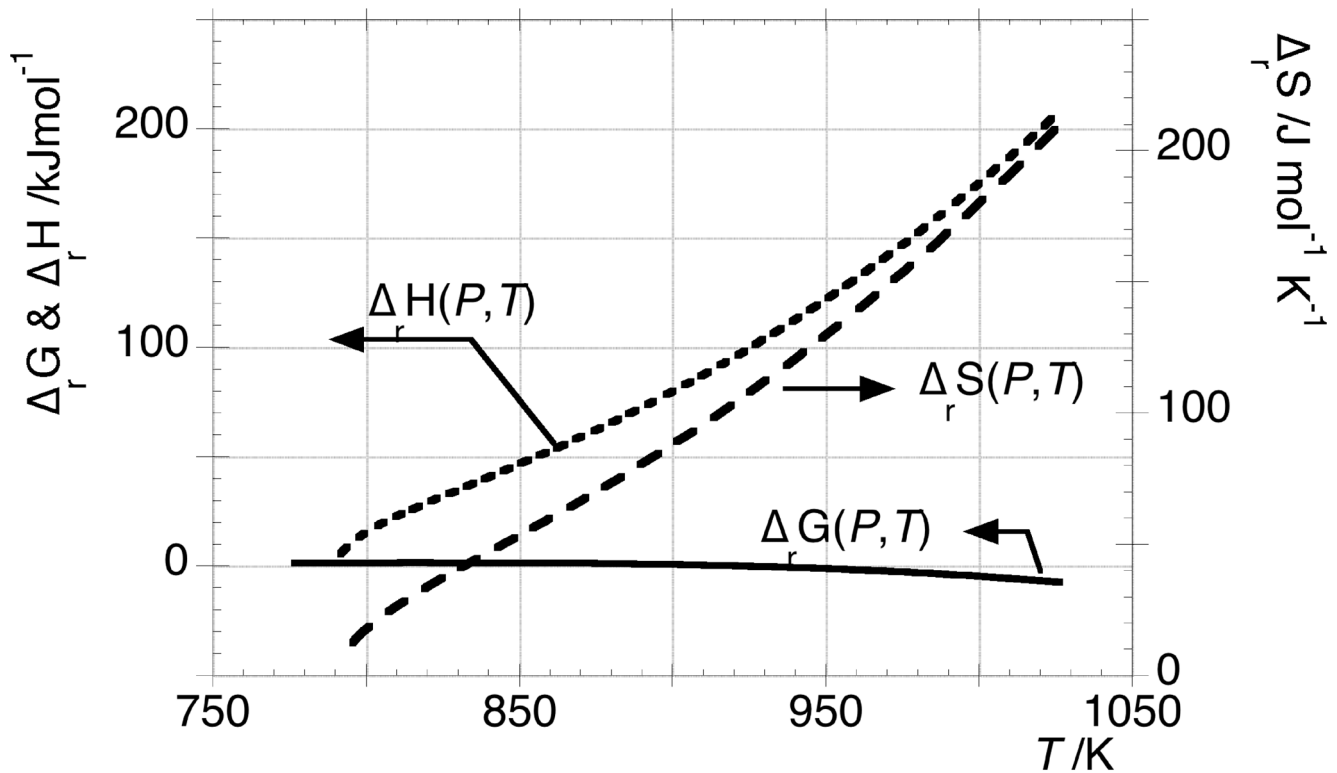doi:10.1371/journal.pone.0105788.g004

Figure 5. Representation on left axis of $\Delta_r H$ and $\Delta_r G$ vs T obtained respectively by eq 7, after solving quadratic equation 13, and eq 1. On the right axis, the trend of $\Delta_r S$ calculated by eq 15 is also displayed.
doi:10.1371/journal.pone.0105788.g005

evidences indicating that the electrode containing OLC is the site where the volume constraint is particularly high. They arise from the comparative analysis of both electrode powder mixtures, before and after the experiments, by making use of x-ray diffraction (XRD), micro Raman spectroscopy (mR) and high-resolution transmission electron microscopy (HR-TEM):

- The XRD patterns spectra demonstrate that no chemical change occurred (see §1.5.1 of the Supporting Information S1). The large increase of crystallinity of CrF_2 was the unique difference found in XRD. Due to their almost amorphous state, OLC give low intensity XRD features differently from HOPG, which is very well revealed. In the present case, the situation is complicated by the presence of features of other species in the electrode that superimpose and/or they are very close to the OLC features (see §1.1.2.2 of the Supporting Information S1). It is reported [20] in high temperature – high pressure experiments on OLC, that their most intense feature ($d_{200} = 0.354$ nm, $2\theta = 24.73°$; see §1.1.2.2 of the Supporting Information S1) is negligibly shifted as function of pressure at constant T. For instance, at 500 °C the lattice parameter changes with pressure as -9.6×10^{-13} nmPa^{-1}. At our calculated pressures, which are in the order of tens of MPa (see below), a shift of $\cong 10^{-5}$nm is expected, which is clearly undetectable. The mR spectroscopy does not reveal differences (see §1.5.2 of the Supporting Information S1) with exception of some changes in the relative intensities, which are meaningless. There is superimposition of the OLC and HOPG features with the features of the mixture Cr_3C_2 - CrF_2 (see §1.1.2.3 of the Supporting Information S1). Therefore, though this inconvenient, the absence of any new feature is a proof that both carbon species remain unchanged;

- HR-TEM and STEM analyses show a very different scenario of the electrode powder with OLC before and after the experiments. Before, OLC are easy identifiable in the mixture as reported in the STEM image of Fig. 6A. Free OLC nanostructures (red arrows) are quite abundant, where they can be seen either as spots with very light contrast on the holey carbon grid or mixed with the Cr_3C_2-CrF_2 powder. The HAADF-STEM mode is also known as Z contrast mode because the intensity in each point of the image is proportional to Z^{α} with $\alpha \sim 2$ and Z the atomic number. Carbon appears dark, as it is much lighter than the other compounds present in these samples. The OLC morphology at the nanoscale is shown in Fig. 6B and is found in agreement with previous experimental results [7][21]. The inset in Fig. 6B shows the Fast Fourier Transform (FFT) of OLC where the reflections of graphitic planes appear quite diffuse.

The powder mixture of the same electrode after the experiment appears completely different: OLC are practically disappeared while large grains with round shaped contours were found as shown in the STEM image in Fig. 7A. Free OLC are hardly observable: just small pieces on the agglomerates, while the holey carbon grid is practically clean. The analysis on the very few OLC found in the sample reveals some significant differences with respect to the OLC before the experiment: the graphitic planes form now better ordered quasi-spherical structures (see Fig.7B). The electron energy loss spectroscopy measurements (see § 1.5.3. of the Supporting Information S1) agree with this result: the sp^2 carbon coordination values were found 82±3% and 86±3% for
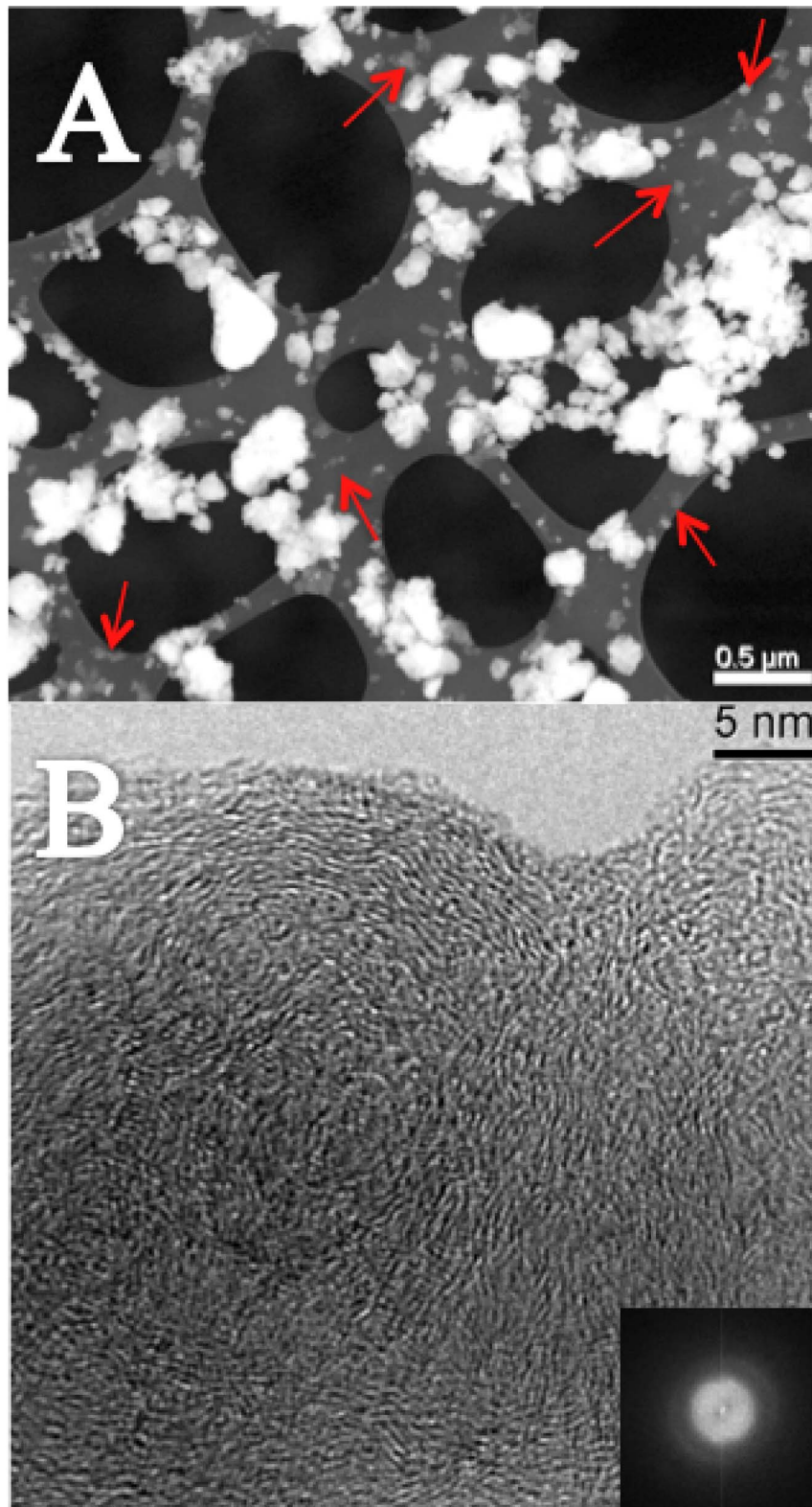
Figure 6. Before the experiment. Panel A: STEM image of the powder of the electrode containing OLC. The OLC nanostructures appear on the holey carbon grid as spot with very light contrast. Some of them are indicated with red arrows. Panel B: HR-TEM of OLC. The FFT image in the inset shows poor crystallinity of OLC.
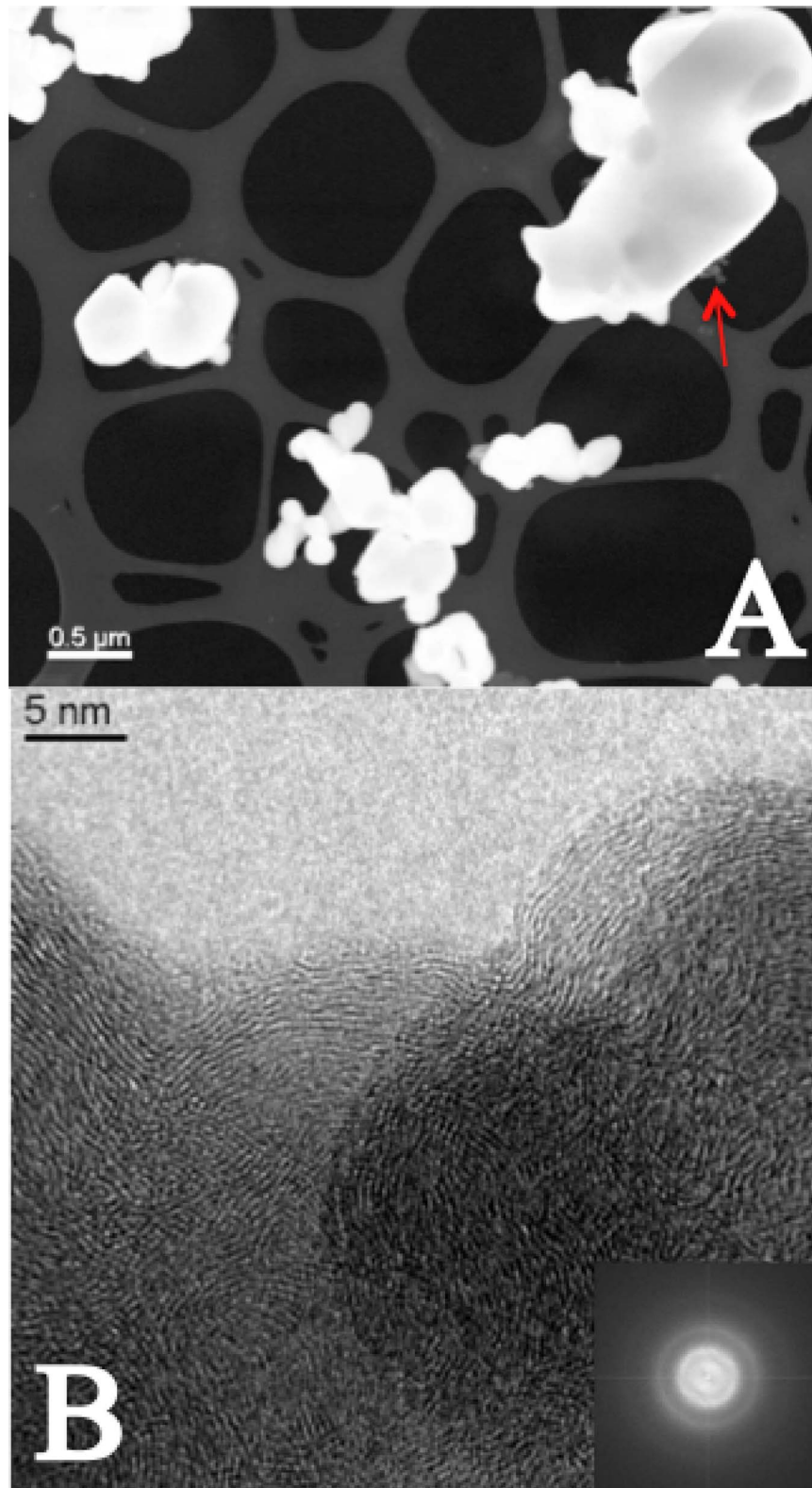doi:10.1371/journal.pone.0105788.g006

Figure 7. After the experiment. Panel A: STEM image of the powder of the electrode containing OLC. The OLC nanostructures are practically disappeared. The holey carbon grid is clean and only large grains with rounded shape stay on the grid. A few visible OLC are indicated with red arrow. Panel B: HR-TEM of OLC. The FFT image in the inset shows that the crystallinity of OLC is higher with respect to the FFT image in Figure 6B.
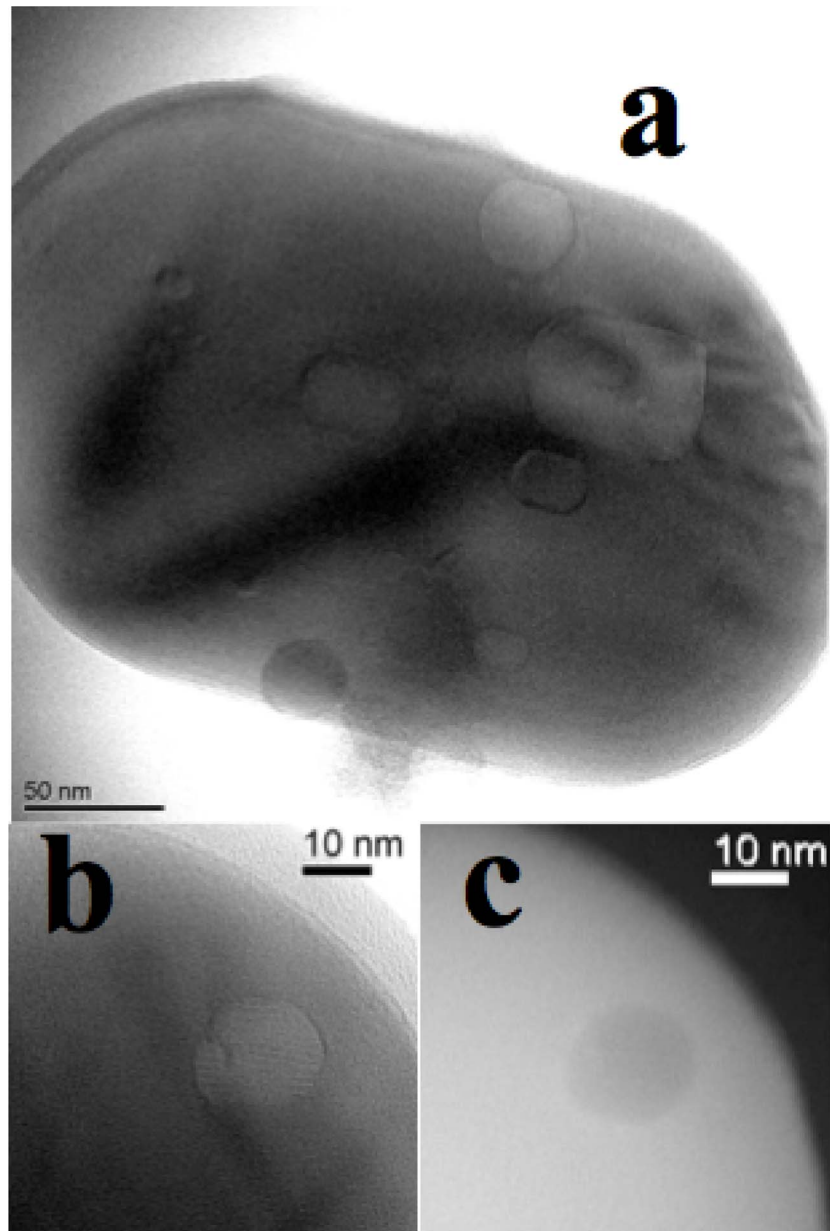doi:10.1371/journal.pone.0105788.g007

Figure 8. Zero loss TEM image (Panel a) of a typical small sintered particle (as the particles in Figure 7A) of the electrode with OLC after the experiment. The particle contains several cavities, that can be empty, or at least full of material much lighter than the surrounding sample, as it is proven by the comparison between the HRTEM (panel **b**) and STEM (panel **c**) images of the same cavity, that is whiter in **b** and darker in **c**.

OLC before and after, respectively and the result seems to point to a further graphitization of OLC towards multishell ordered structures in the process (see discussion below). The sintered agglomerates usually are so thick to result non-transparent to electrons and to prevent the analysis of their internal structure. When small particles are found, the EELS revealed typical features of variable size inside the particle. Their contrast is typical of cavities, but it was not possible to assess whether they are empty or possibly filled with OLC. This is the most reasonable hypothesis, being OLC otherwise missing.

The zero loss TEM image of a typical small sintered particle containing several cavities is shown in Fig. 8a. The fact that these cavities are empty or filled with material lighter than the surrounding sample is proven by the comparison between the HRTEM and STEM images in Fig. 8b and Fig. 8c of the same cavity, that is whiter in b and darker in c.

The electrode containing HOPG and the same Cr_3C_2 - CrF_2 mixture does not show any modification after the experiment, as it can be seen by comparing the STEM images in Fig.9 A and B.

The following considerations arise from the above evidences:

- The temperature range explored in the experiments does not allow suspecting any vaporization of carbon from OLC. The C-nanostructures are still in the electrode;

- High temperatures and experiments lasting hundreds of hours create the ideal conditions to favour the sintering of the whole
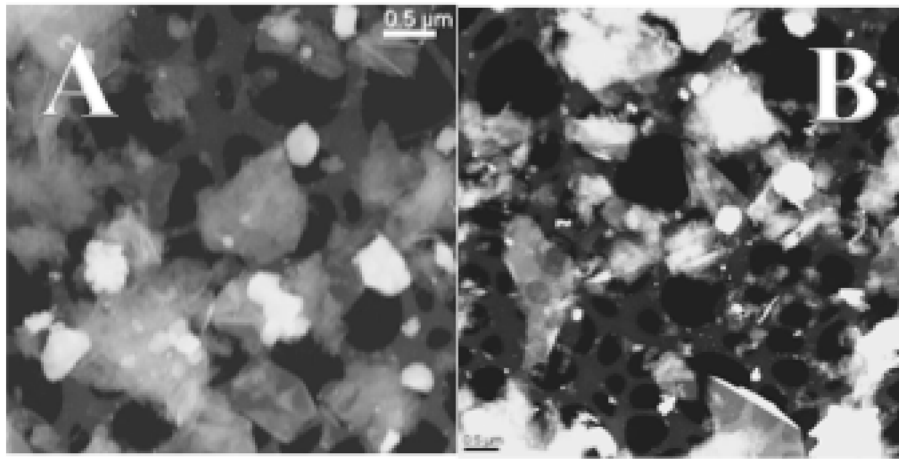
Figure 9. STEM images of the electrode containing HOPG. Panel A, **before the experiment**. Panel B, **after the experiment**. No differences were found and no sintering was observed.
doi:10.1371/journal.pone.0105788.g009

mixture where OLC remain embedded in the very hard and refractory structure of Cr_3C_2. The melting points of Cr_3C_2 and CrF_2 are respectively 2168 and 1167 K. The highest temperature reached in the experiments was 1030 K, which is close to the melting point of CrF_2. Thus, it is expected that its softening acts as a sintering medium of the whole mixture. The high specific surface area of OLC (>100 m^2g^{-1}, see § 1.1.1 of the Supporting Information S1) contributes to this process and facilitates the embedding of the nanostructure. Therefore, the role of OLC nanoparticles seems to be crucial and it explains the absence of any modification of the electrode containing HOPG (and the same Cr_3C_2-CrF_2 mixture) which worked in the same experimental conditions;

- Consider as rough approximation the electrodes as cylinders free of expanding with temperature filled with rigid particles (sintered Cr_3C_2-CrF_2 mixture) embedding nanoparticles (OLC) the dilatation of which is hindered. By imposing no volume change for both OLC and HOPG, the respective $\frac{dP}{dT} = \frac{\alpha}{\kappa}$ values can be evaluated and compared as follows:

$$\left.\frac{dP}{dT}\right|_O = \left(\frac{\alpha}{\kappa}\right)_O \cong 0.5\,\text{MPaK}^{-1}; \left.\frac{dP}{dT}\right|_H = \left(\frac{\alpha}{\kappa}\right)_H \cong 8\,\text{PaK}^{-1} \quad (16)$$

The subscripts O and H stand for OLC and HOPG. The temperature dependence of the quantities entering eq 16 has been neglected in the computation and the coefficients a_2, b_1, c_0 and d_0 were only retained in the expression reported in Table 3. The values found in eq 16 demonstrate clearly the great difference in the internal pressures to which both carbon forms are subjected in the respective electrodes. For the sake of comparison, the quantity $\frac{dP}{dT}$ for Cr_3C_2 is: $\left.\frac{dP}{dT}\right|_{Cr} = \left(\frac{\alpha}{\kappa}\right)_{Cr} \cong 3.4\,\text{MPaK}^{-1}$ where κ [22] and α [23] are available in literature. Due to the negligible changes with temperature of the internal pressure (see eq 16), the chemical potential of carbon in HOPG, μ_H, is only a function of T differently to the chemical potential of carbon in OLC, μ_O, that is a function of T and $P(T)$. Therefore, we can write that:

$$\Delta_r G(T,P) = \mu_O[T,P(T)] - \mu_H(T). \quad (17)$$

Evaluation of the surface contribution

Owing to the nanometric size of the carbon particles, the surface contribution to the energetics of the process cannot be neglected, in principle. In the following of this section the shape of the nanoparticle is assumed to be spherical. Let us estimate the chemical potential difference using the thermodynamic approach, based on the Gibbs model for interface [24], in terms of bulk chemical potential, surface free energy and surface tension.

The difference between surface energy and surface tension plays a fundamental role when dealing with interphases in the solid state. In this respect, we briefly recall the definition of these quantities, which are needed for the discussion that follows. The surface energy excess, σ, is the reversible work required to create a unit surface at constant volume, temperature, pressure and composition [24]. In such a process the surface is not stretched during its formation. On the other hand, the surface tension, γ, is defined as the reversible work (per unit area) required to change the area of the surface through a stretching process. It is worth noticing that in this definition the infinitesimal deformation of the surface involves an "initial" configuration of the system where the solid is not stressed. By including bulk and surface contributions, the general expression of the chemical potential difference reads (see §2 of the Supporting Information S1)

$$\Delta_r G(T) = \Delta\mu_B + \Delta\mu_S = \Delta\mu_B + \frac{2V}{r}\left(\sigma - \frac{\kappa\gamma^2}{3r}\right) \quad (18)$$

where r is the radius of the nanoparticle and $\Delta\mu_B$ denotes the "bulk" contribution, that is $\Delta\mu_{r\to\infty}$. In the following we focus our attention on the impact of the surface term ($\Delta\mu_S$) on $\Delta_r G(T)$ and on its temperature dependence.

The contribution of the surface tension containing term to $\Delta\mu_S$ is usually smaller than that due to the surface excess free energy, $\frac{2V\sigma}{r}$. Consequently, $\Delta\mu_S$ is expected to be higher than zero. Typical values of the quantities entering eq 18 are [25]

$V = 5.36 \times 10^{-6}$ m^3 mol^{-1}, $\kappa = 3.24 \times 10^{-10}$ Pa^{-1} and $r = 10$ nm. As far as the σ value is concerned, for nanocarbon structures, such as fullerene, single and multi walled nanotubes, it is found [5] to range between 0 and 0.045 Jm^{-2}. On this basis, the upper bound of $\Delta\mu_S \cong \dfrac{2V\sigma}{r}$ is estimated to be about 50 Jmol^{-1} for $r = 10$ nm.

As far as the temperature dependence of $\Delta\mu_S$ is concerned, it is ascribed to the temperature dependence of the physical quantities entering in eq 18. In particular, the temperature dependence of σ is given by the Gibbs adsorption equation that, for one component system, implies $\dfrac{d\sigma}{dT} = -s^x$, where $s^x = S^x/A$ is the excess surface entropy. From this equation, neglecting as a first approximation the temperature dependence of the excess entropy in the temperature range here considered, we get $\sigma(T) = -s^x(T - T*) + \sigma*$ where $T*$ is the temperature at which $\Delta_r G(T) = 0$. Concerning the temperature dependence of the surface tension, given by eq 1 in the Supporting Information S1 (§ 2), it is obtained

$$\frac{d\gamma}{dT} = -s^x - A\frac{d_s s^x}{d_s A} + \frac{2}{3}\alpha\gamma \qquad (19)$$

where we exploit the fact that the surface energy is a function of the independent variables temperature and "stretched area" A (the subscript s stands just to remind us that the variation is performed by stretching). According to the discussion that follows this derivative can be estimated using the Born-Stern method [26]. In this approach, the entropy excess per unitary area of a solid-vacuum interface is equal to $s^x = \dfrac{1}{A}\left(S - S'\right) = \rho_a\left(s_1 - s_1'\right)$ where S is the entropy of the actual solid, S' the entropy of the model system (without interface), ρ_a the surface density and $s_1\left(s_1'\right)$ the entropy, per atom, of surface (bulk) species. By assuming, as usual, $\left(s_1 - s_1'\right)$ independent of temperature and deformation of the surface $\dfrac{d_s A}{A}$, for $\dfrac{d_s\rho_a}{d_s A} = -\dfrac{\rho_a}{A}$ one obtains $\dfrac{d\gamma}{dT} = -s^x - A\left(s_1 - s_1'\right)\dfrac{d_s\rho_a}{d_s A} + \dfrac{2}{3}\alpha\gamma \cong \dfrac{2}{3}\alpha\gamma$. For instance, by considering the excess entropy equal to the change in the vibrational entropy of the atom the expression $s^x \cong k\rho_a \ln\dfrac{v_\perp}{v_\perp'}$ holds where $v_\perp'(v_\perp)$ is the vibrational frequency of the surface (fully coordinated) atom along the "broken bond" direction. Since for the number of mole of atoms in the particle, N, is constant we set $\dfrac{r^3}{V} = \dfrac{3}{4\pi}N = b^{-1}$ in eq 18 to obtain $\Delta\mu_S = 2br^2\left(\sigma - \dfrac{\kappa\gamma^2}{3r}\right)$. Moreover,

$$\frac{d\Delta\mu_S}{dT} \cong -2\frac{V}{r}\left[s^x - \frac{\alpha}{3}\left(2\sigma - \frac{5}{3}\frac{\kappa\gamma^2}{r}\right)\right] \qquad (20)$$

where α is of the order of 10^{-6} K^{-1}. A crude estimate of the vibrational contribution of s^x, on the basis of the Kossell model [26] shows that $s^x > k\rho_a \ln\sqrt{2}$ that implies, using $\rho_a = \rho_g^{\frac{2}{3}}$ with ρ_g
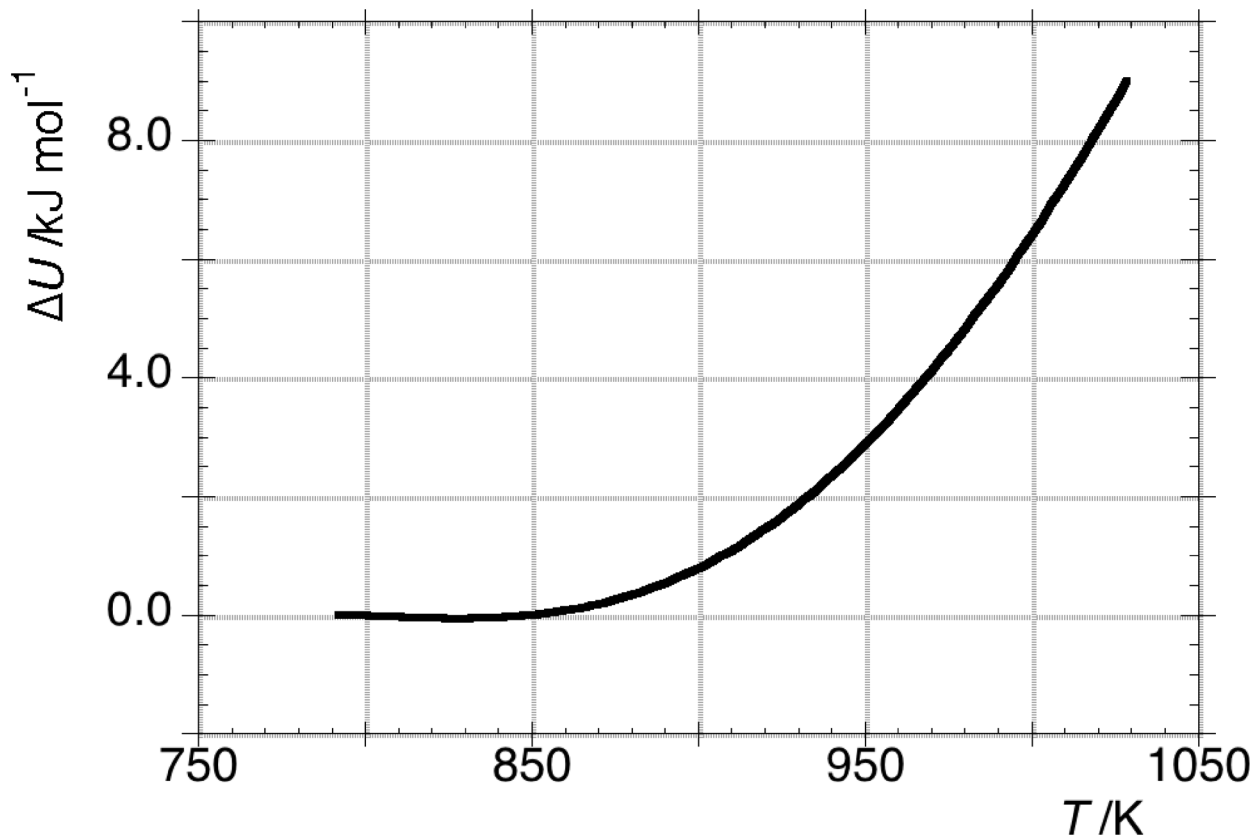

Figure 10. The change of internal energy $\Delta U[T, P(T)]$ of OLC is reported against temperature according to eq 22.
doi:10.1371/journal.pone.0105788.g010

the graphite density, a value of $s^x \geq 10^{-4}$ J m^{-2} K^{-1}. This figure is about two orders of magnitude larger than α. Moreover, $(2Vs^x/r)_{r=10\text{nm}} \geq 0.1$ J mol^{-1} K^{-1}. From eq 15, the value of $\Delta_r S(P,T)$, in the middle of temperature range, is equal to 96.75 Jmol^{-1}K^{-1}, which is not consistent with the value $(-2Vs^x/r)$.

The present analysis indicates that the bulk term is the dominant contribution both to the chemical potential change of transformation B and its derivative on T. At this point, a comment is in order on the use of the Gibbs model for dealing with OLC systems. In fact, in this approach "bulk" and surface terms sum up as two independent contributions where the "size effect" is usually contained in the surface term only, i.e., $\Delta\mu_B = \Delta\mu_{r\to\infty}$ is independent of r. On the other hand - still remaining in the framework of the Gibbs model - owing to the variable curvature of the sheets, which made up the nanoparticles, in the OLC the "bulk" term has to be considered a function of the particle radius. For this reason in the following we refer to "atomistic" approaches for determining the energetics of the OLC particles. In fact, in these methods a suitable interaction potential functions for the C atoms is used and this makes it possible to estimate $\Delta\mu_B$ as a function of r.

Now we focus our attention on the internal energy of the particle due to the isothermal transformation from a relaxed state at internal energy U_0 and volume V_0 to a stressed state at U and V. To do this the *energy equation*, namely

$$\left(\frac{\partial U}{\partial V}\right)_T = T\left(\frac{\alpha}{\kappa}\right) - P \tag{21}$$

was utilized. The integration of eq 21 gives the change of internal energy as (see §3 of the Supporting Information S1):

$$\Delta U = (U - U_0)_T = \frac{V^0}{\kappa}\left\{\left[1 - (1+\kappa P)e^{-\kappa P}\right] + \alpha T\left(e^{-\kappa P} - 1\right)\right\} \tag{22}$$

The value of V^0, α and $\kappa\kappa$ are given in Tables 2 and 3. The pressure as function of T was obtained by numerical integration of $\frac{dP}{dT} = f(T)$ assuming $P = 0$ at $T = 776.6$ K, which was the lowest experimental temperature. The resulting function satisfies the relationship $P = m_0 + m_1 T + m_2 T^2 + m_3 T^3$ where $m_0 = 1.2947 \times 10^6$ bar; $m_1 = -4187.2$ bar K^{-1}; $m_2 = 4.2571$ bar K^{-2}; $m_3 = -1.3067 \times 10^{-3}$ bar K^{-3} with correlation coefficient 0.9999. At the highest temperature, the maximum pressure value is about 70 kbar. The trend of $\Delta U[T,P(T)]$ with temperature, which is almost perfectly quadratic, is plotted in Fig. 10.

It is worth noticing that the $\Delta U[T,P(T)]$ values and its trend with temperature are not comparable with values and trend of $\Delta_r H(P,T)$ reported in Fig. 5. For example, at 903 K, which is the temperature in the middle of the explored temperature interval, the ratio $\frac{\Delta_r H(P,T)}{\Delta U[T,P(T)]} \cong 10^2$.
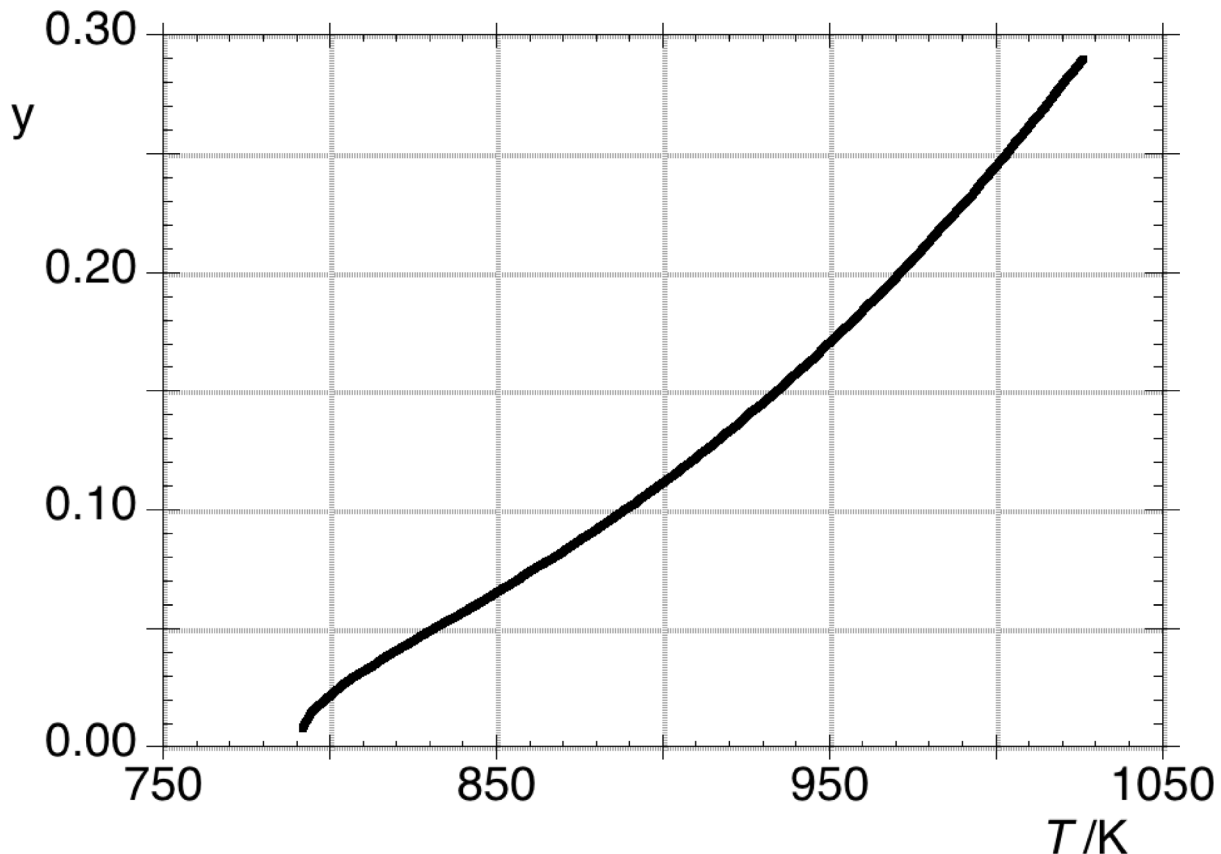

Figure 11. Trend of the change of the fraction of C defects in OLC against T. One assumes that the real transformation involves equilibrium $C_{HOPG} = C_{OLC_x} = yC_{ad} + C_{OLC_{x-y}}$ and y is calculated by eq 23.
doi:10.1371/journal.pone.0105788.g011

Due to such a high ratio jointly to the very small surface contribution, we assume that as a consequence of the high internal pressure another process connected to B should be considered. We are likely dealing with a reversible process that requires the formation of C defects in OLC, probably already defective. Thus, the whole process determining the *emf* of the cell could be written as:

$$C_{HOPG} = C_{OLC_x} = yC_{ad} + C_{OLC_{x-y}} \qquad (B1)$$

instead of process B.

Obviously, this implies that the previously considered relation $\Delta_r G = \mu_O - \mu_H$ should be written as $\Delta_r G = <\mu_O> - \mu_H$ where $<\mu_O>$ is the mean chemical potential of carbon atoms in the electrode containing the OLC nanostructures. In this quantity, the C atoms formed should be considered adsorbed atoms, C_{ad} the formation of which causes dangling bonds. A rough evaluation of the defect fraction in equilibrium B1 can be evaluated through equation:

$$y = \frac{\Delta_r H(P,T) - \Delta_f H_{O_{x-y}}}{\Delta_f H_C} \cong \frac{\Delta_r H(P,T)}{\Delta_f H_C} \qquad (23)$$

where $\Delta_f H_C$ and $\Delta_f H_C$ are the enthalpy of formation per carbon atom of defective OLC and free carbon atom (7.43 eV at 298 K) [27], respectively. The quantity $\Delta_f H_{O_{x-y}}$ depends on the number of shells as described for multishell fullerene (MSF) made of concentric circumspheres of polyhedra C_n (I_h, $n = 60k^2$) and C_n (I_h, $n = 180k^2$) where $k = 1,2$ up to L is any positive integer representing the number of shells. I_h and n are respectively the symmetry group and number of C atoms. According to the literature [28], the quantity $\Delta_f H_{O_{x-y}}$ is of the order of magnitude of meV and therefore it is negligible when compared to $\Delta_r H(P,T)$ which is about 1 eV. Even the formation energy of a single carbon shell starting from graphene implies negligible energy values ranging from 331 to 34 meV at^{-1} for C_{60} and C_{960}, respectively (see J. Bernholc et al. [3]). As stated in the above reference, the authors showed that the larger the size of the shell, the lower the energy of formation. Figure 11 shows how y changes with T.

Due to the assumption for obtaining eq 23, the trend of y is the same as $\Delta_r H(P,T)$ shown in Fig. 5. Anyway, the value of y is likely consistent with a change corresponding to one or more OLC shells. The experimental evidence through the *emf* vs T data shows that this process occurs reversibly. In addition, defects imply the formation of dangling bonds, which also contribute to the increase of the entropy change.

Conclusions

In the present experimental work, we obtained high temperature data of the stability of onion-like carbon with respect to highly oriented pyrolytic graphite. Since this was performed in reversible way, through the *emf* measurement of a galvanic cell, the quantities related to the transformation investigated have to be considered reliable thermodynamic data.

The evidence that in the operating conditions the *emf* data cannot be only function of temperature allowed measuring the changes of the chemical potential of carbon in OLC under volume constraint. The volume constraint is reasonably proven by the HR-TEM images where the rigid cages made of sintered CrF_2–Cr_3C_2 mixture likely embed OLC.

The positive value of $\Delta_r S$ and its increase with temperature indicate that the OLC is a nanostructured system with a large number of defects. The change of their fraction with T was evaluated. The present analysis indicates that the bulk term is the dominant contribution to both chemical potential and entropy change of the transformation.

The absence of any chemical change in the electrodes after hundreds hours of work at high temperature guarantees the whole reliability of the experiments.

Supporting Information

Supporting Information S1
(DOC)

Author Contributions

Conceived and designed the experiments: AL D. Gozzi. Performed the experiments: AL D. Gozzi LL GB D. Gazzoli LB. Analyzed the data: D. Gozzi MT. Contributed reagents/materials/analysis tools: AL. Contributed to the writing of the manuscript: D. Gozzi MT. Galvanic cell and experiment preparation, emf measurements, data elaboration: AL LB D. Gozzi. Evaluation of surface contribution and discussion of results: MT. HRTEM and EELS measurements: LL GB. microRaman measurements: D. Gazzoli.

References

1. Gozzi D, Latini A, Lazzarini L (2009) High-temperature determination of surface free energy of copper nanoparticles. J Am Chem Soc 131: 12474–12482.
2. Tomanek D, Zhong W, Krastev E (1993) Stability of multishell fullerenes *Phys Rev B* 48: 15461–15464.
3. Bernholc J, Brabec CJ, Maiti A, Yi J-Y (1994) Structural transformations, reactions, and electronic properties of fullerenes, onions, and buckytubes. Comp Mat Science 2: 547–556.
4. Girifalco LA, Hodak M, Lee RS (2000). Carbon nanotubes, buckyballs, ropes, and a universal graphitic potential. Phys Rev B 62: 13104–13110.
5. Jiang Q, Chen ZP (2007) Thermodynamic phase stabilities of nanocarbon. Carbon 44: 79–83.
6. Barnard AS (2006) Theory and modeling of nanocarbon phase stability. Diamond & Related Mat 15: 285–291.
7. Banhart F, Ajayan PM (1996) Carbon onions as nanoscopic pressure cells for diamond formation. Nature 382: 433–435.
8. Banhart F, Füller T, Redlich Ph, Ajayan PM (1997) The formation, annealing and self-compression of carbon onions under electron irradiation. Chem Phys Lett 269: 349–355.
9. Sun L, Banhart F (2006) Graphitic onions as reaction cells on the nanoscale. Appl Phys Lett 88: 193121–193123.
10. Latini A, Gozzi D, Ferraris G, Lazzarini L (2011) High-temperature resistivity of dense mats of single-walled carbon nanotube bundles. J Phys Chem C 115: 11023–11029.
11. Latini A, Tomellini M (2009) Thermodynamics of CVD synthesis of multiwalled carbon nanotubes: a case study. J Phys Chem C 113: 45–53.
12. Gozzi D, Iervolino M, Latini A (2007) The thermodynamics of the transformation of graphite to multiwalled carbon nanotubes. J Am Chem Soc 129: 10269–10275.
13. Shenderova OA, Zhirnov VV, Brenner DW (2002) Carbon nanostructures. Crit Rev Solid State Mater Sci 27; 227–356.
14. Kuznetsov VL, Chuvilin AL, Butenko YV, Mal'kov IY, Gutakovskii AK, et al. (1994) Study of onion-like carbon OLC formation from ultra disperse diamond (UDD). Mater Res Soc Symp Proc 359: 105–110.
15. Lee RKF, Hill JM (2012) General formulae for interacting spherical nanoparticles and fullerenes. J Math Chem 50: 1289–1303.
16. Zaiser M, Banhart F (1997) Radiation-induced transformation of graphite to diamond. Phys Rev Lett 79: 3680–3683.
17. Klotz IM, Rosemberg RM (2008) Chemical Thermodynamics. 7th Edition, John Wiley & Sons, Inc., Publishing, p. 200.
18. Girifalco LA (1995) Extended Mie-Grüneisen theory applied to C60 in the disordered fcc phase. Phys Rev B 52: 9910–9916.

19. Sano N, Wang H, Alexandrou I, Chhowalla M, Teo KBK, et al. (2002) Properties of carbon onions produced by an arc discharge in water. J Appl Phys 92: 2783–2788.

20. Dubitsky GA, Serebryanaya NR, Blank VD, Skryleva EA, Kulnitsky BA, et al. (2011) Effect of high pressures and temperatures on carbon nanoonion structures: comparison with C60. Russ Chem Bull Int Ed 60: 413–418.

21. Welz S, McNallan MJ, Gogotsi Y (2006) Carbon structures in silicon carbide derived carbon. J Mat Proc Tech 179: 11–22.

22. Chao J (2008) First-principles study of structural, elastic, and electronic properties of chromium carbides. Appl Phys Lett 92: 041909–041911.

23. Scabarozi TH, Amini S, Leaffer O, Ganguly A, Gupta S, et al. (2009) Thermal expansion of select $Mn+1AXn\ M$ = early transition metal, A = A group element, X = C or N) phases measured by high temperature x-ray diffraction and dilatometry. J Appl Phys 105: 013543–0135410.

24. Shuttleworth R (1950) The Surface Tension of Solids. Proc Phys Soc (London) A 63: 444–457.

25. Colonna F, Fasolino A, Meijer EJ (2011) High-pressure high-temperature equation of state of graphite from Monte Carlo simulations. Carbon 49: 364–368.

26. Mutaftschiev B (2001) The atomistic Nature of Crystal Growth. Springer-Verlag.

27. IVTANTHERMO for Windows, v.3.0; database of thermodynamic properties of individual substances and thermodynamic modeling software; Glushko Thermocenter of RAS: 2005

28. Tang AC, Huang FQ (1995) Theoretical studies of multishell fullerenes. Phys Rev B 52: 17435–17438.